

Gravitational wave production by Hawking radiation from rotating primordial black holes

Ruifeng Dong, William H. Kinney, Dejan Stojkovic

HEPCOS, Department of Physics, SUNY, University at Buffalo, Buffalo, NY 14260-1500

In this paper we analyze in detail a rarely discussed question of gravity wave production from evaporating primordial black holes. These black holes emit gravitons which are, at classical level, registered as gravity waves. We use the latest constraints on their abundance, and calculate the power emitted in gravitons at the time of their evaporation. We then solve the coupled system of equations that gives us the evolution of the frequency and amplitude of gravity waves during the expansion of the universe. The spectrum of gravitational waves that can be detected today depends on multiple factors: fraction of the total energy density which was occupied by primordial black holes, the epoch in which they were formed, and quantities like their mass and angular momentum. We conclude that very small primordial black holes which evaporate before the big-bang nucleosynthesis emit gravitons whose spectral energy fraction today can be as large as $10^{-7.5}$. On the other hand, those which are massive enough so that they still exist now can yield a signal as high as $10^{-6.5}$. However, typical frequencies of the gravity waves from primordial black holes are still too high to be observed with the current and near future gravity wave observations.

PACS numbers:

I. INTRODUCTION

Gravity waves are the last prediction of the general theory of relativity that has recently been verified by LIGO/Virgo collaborations [1, 2]. Many dynamical systems are capable of producing gravity waves, in particular mergers of black holes (BHs) or neutron stars. It is also believed that primordial gravity waves can be produced in the early universe by tensor mode fluctuations during inflation, second-order effects of scalar perturbations [3, 4], or by phase transitions. Another mechanism that has not been extensively studied in the literature is the BH evaporation. BH evaporation is close to thermal. This means that all the degrees of freedom whose mass is smaller than the BH temperature will be democratically excited. Among the other degrees of freedom, gravitons will be excited too. These gravitons at the classical level are nothing else but gravity waves. Therefore, primordial black holes (PBHs) [5–9] evaporation is one of the possible sources of gravity waves. This was studied for the first time in [10].

PBHs can form in the collapse of density fluctuations in the radiation-dominated universe (caused for example by some violent processes like phase transitions). This collapse is possibly anisotropic, producing rotating Kerr PBHs. Even if the collapse is perfectly spherically symmetric and the resulting black hole is Schwarzschild, any subsequent accretion of the surrounding material will introduce non-zero angular momentum. Accretion is very efficient in spinning up the BHs. The amount of accreted mass which is comparable to the initial BH mass is sufficient to spin up the BH from a non-rotating state to almost extremal Kerr state. This is especially important when we study PBH in a higher mass range (i.e. $> 10^{15}$

g) since their lifetime is comparable to or larger than the life-time of the universe, so they have enough time to significantly spin up. It is therefore instructive to study the effect of BH rotation to the spectrum of emitted gravitational waves. In this paper we will, for the first time, calculate the possible gravity wave signals from rotating PBHs.

The thermal black body spectrum of particles emitted from BHs is modified by greybody factors, which quantify the probability that a created particle will penetrate the potential barrier and reach a distant asymptotic observer. Greybody factors can in certain cases modify the spectrum very significantly. For example, it is known that a non-rotating Schwarzschild BHs preferably emit particles of lower spin (e.g. scalars), while emission of particles with higher spin (e.g. gravitons) is suppressed. In contrast, a rotating Kerr BHs preferably emit gravitons. The reason is that emission of higher spin modes from BHs gets amplified taking away rotational energy of BHs. This amplification enhances the probability of graviton emission by many orders of magnitude. The typical energy of the particles (scalar, spinor, vector or tensor) is also larger in the emission from faster rotating BHs. This enhanced emission in turn shortens the lifetime of BHs. Therefore, the greybody factor calculation is important to get the gravity wave signals from evaporating Kerr PBHs.

In this paper, we extend the analysis performed in [10] in two ways. In order to study the effects of BH rotation, we first calculate the greybody factors in section II, and thus the gravity wave spectrum at emission time in section III. The evolution of the PBH parameters like mass and angular momentum is then also computable, as shown in section IV. Second, we discuss the physical

requirements in choosing parameters in section V. The effects of cosmic expansion on the observed signal is derived in section VI. After completing this preliminary setup, we perform our calculations of gravity wave spectrum for small PBHs that evaporate before the big-bang nucleosynthesis (BBN) in section VII. In addition, after taking into account the observational astrophysical limits (summarized in section VIII) we also compute the gravity wave spectrum for larger black holes that evaporated before or are still evaporating today in sections IX. The results are summarized in section X. Throughout the paper we use Planck units, i.e. $\hbar = c = G = k_B = 1$, unless otherwise specified.

II. GREYBODY FACTORS FOR TENSOR MODES

Greybody factors are essential in our analysis for two reasons. First, being the transmission probability over the gravitational potential barrier, they are directly related to the graviton spectrum, as will be shown explicitly in section III. Second, BHs evolve through evaporation by emitting particles of all kinds, i.e. scalars, spinors, vectors and tensors. Unfortunately, [11] only gave partial results for tensor emission spectrum, and [12] calculated the BH's emission into only spinor, vector and tensor modes. The scalar case was considered much later by [13]. Therefore, we will formulate the computation for tensors in this section, and then display our results for the graviton spectrum in the following section.

Throughout the paper, we will consider a general Kerr BH, with the gravitational radius r_+ (which is the outer event horizon size), mass M , angular momentum J , and no electric charge. The dimensionless angular momentum $a_* \equiv J/M^2$ is also frequently used. In the Boyer-Lindquist coordinates (t, r, θ, φ) , the tensor field ψ with energy ω and magnetic quantum number m can be decomposed as

$$\psi = e^{-i\omega t + im\varphi} S(\theta) R(r), \quad (1)$$

The Teukolsky master equations [14] for this field in the background of the Kerr BH are

$$\Delta^2 \frac{d}{dr} \left(\frac{1}{\Delta} \frac{dR}{dr} \right) + \left(\frac{K^2 + 4i(r-M)K}{\Delta} - 8i\omega r - \lambda \right) R = 0, \quad (2)$$

$$\frac{1}{\sin \theta} \frac{d}{d\theta} \left(\sin \theta \frac{dS}{d\theta} \right) + \left[(2 + a_* M \omega \cos \theta)^2 - (m \csc \theta - 2 \cot \theta)^2 - 4 + E \right] S = 0, \quad (3)$$

where $\Delta \equiv r^2 - 2Mr + a_*^2 M^2$, $K \equiv (r^2 + a_*^2 M^2)\omega - a_* M m$, $\lambda \equiv E + a_*^2 M^2 \omega^2 - 2a_* M m \omega - 2$, and $E = {}_2E_l^m(a_* M \omega)$ is to be determined from the eigenvalues of the function $S(\theta)$. l is the angular momentum quantum number, no smaller than $\max(|m|, |s|)$.

The above angular equation (Eq. (3)) is the well-known spin-weighted spheroidal wave equation (spin-2). References [15, 16] used Jacobian polynomial expansion to calculate the eigenvalues ${}_sE_l^m$ to the 6th order of $\gamma \equiv a_* M \omega$, for any spin s . This gives us a precision better than $\frac{1}{10^4}$ for $M\omega \leq 3$. The results are summarized in App. A. However, nontrivial calculation is needed for the radial equation (Eq. (2)), which does not have analytical solutions, so numerical analysis is needed. We are interested in the greybody factors, which give the transmission probability seen by an asymptotic observer if we consider a purely outgoing flux at infinity. Equivalently, by time reversal symmetry, this is the absorption probability by the BH if we consider a purely ingoing flux at its horizon [17]. As usual, we adopt the latter interpretation in the following calculations.

The boundary conditions appropriate for our study are then

$$R \sim \Delta^2 e^{-ikr^*}, \quad r \rightarrow r_+, \quad (4)$$

$$R \sim Z_{in} r^{-1} e^{-i\omega r^*} + Z_{out} r^3 e^{i\omega r^*}, \quad r \rightarrow \infty, \quad (5)$$

where $k \equiv \omega - m\Omega$, $\Omega \equiv a_*/(2r_+)$ is the angular velocity of the horizon, and r^* is defined by $\frac{dr^*}{dr} = \frac{r^2 + a_*^2 M^2}{\Delta}$. Z_{in} and Z_{out} are constants to be found from numerical integration of Eq. (2) once we fix the boundary solution near the horizon as (4). At the two boundaries, the field energy fluxes are [11]

$$\frac{d^2 E_{hor}}{dtd\Omega_3} = \frac{{}_2S_{lm}^2(\theta)}{2\pi} \frac{128\omega k(k^2 + 4\epsilon^2)(k^2 + 16\epsilon^2)(2Mr_+)^5}{|C|^2}, \quad r \rightarrow r_+ \quad (6)$$

$$\frac{d^2 E_{out}}{dtd\Omega_3} = \frac{{}_2S_{lm}^2(\theta)}{2\pi} \frac{1}{2\omega^2} |Z_{out}|^2, \quad r \rightarrow \infty \quad (7)$$

$$\frac{d^2 E_{in}}{dtd\Omega_3} = \frac{{}_2S_{lm}^2(\theta)}{2\pi} \frac{128\omega^6}{|C|^2} |Z_{in}|^2, \quad r \rightarrow \infty, \quad (8)$$

where $\epsilon \equiv \sqrt{1 - a_*^2}/(4r_+)$, and

$$|C|^2 = (Q^2 + 4a_* M \omega m - 4a_*^2 M^2 \omega^2) [(Q - 2)^2 + 36a_* M \omega m - 36a_*^2 M^2 \omega^2] + (2Q - 1)(96a_*^2 M^2 \omega^2 - 48a_* M \omega m) + 114M^2 \omega^2 (1 - a_*^2), \quad (9)$$

with $Q \equiv {}_2E_l^m + a_*^2 M^2 \omega^2 - 2a_* M \omega m$. Here Ω_3 is the solid angle in 3-dimensional space and ${}_2S_{lm}(\theta)$ is the normalized eigenfunction of Eq. (3), which does not concern us here. The field absorption probability is

$$\begin{aligned} \gamma_{2lm}(a_*, M\omega) &\equiv 1 - \frac{d^2 E_{out}}{dtd\Omega_3} \bigg/ \frac{d^2 E_{in}}{dtd\Omega_3} \\ &= \frac{d^2 E_{hor}}{dtd\Omega_3} \bigg/ \left(\frac{d^2 E_{hor}}{dtd\Omega_3} + \frac{d^2 E_{out}}{dtd\Omega_3} \right) \\ &= \frac{128\omega k(k^2 + 4\epsilon^2)(k^2 + 16\epsilon^2)(2Mr_+)^5}{128\omega k(k^2 + 4\epsilon^2)(k^2 + 16\epsilon^2)(2Mr_+)^5 + \frac{|C|^2}{2\omega^2} |Z_{out}|^2}. \end{aligned} \quad (10)$$

In the numerical calculation, we set our scale by letting $r_+ = 1$. After imposing the solution (4) at $r = 1 + 10^{-3}$,

we integrate (2) to larger r , until the solution becomes stable, in practice at $r = 10^3$. The r^3 term dominates $R(r)$ there, so the factor Z_{out} is easily obtained. The greybody factor is then computed using Eq. (10) for any mode (ω, l, m) .

III. INSTANTANEOUS GRAVITON SPECTRUM

Two factors are affecting the graviton spectra that we can observe today. One is the Hawking spectrum of a PBH with fixed mass M and angular momentum J , and the other is the evolution of M and J in the expanding universe. Here we focus on the former, and the latter is dealt with in the next section.

We first define a dimensionless quantity $Q^{GW}(a_*, M\omega)$, which represents the expected emission rate, i.e. the number of particles emitted per unit frequency per unit time, for gravitons. This quantity includes blackbody and greybody terms which are uniquely determined with two dimensionless parameters $a_* \leq 1$ and $x \equiv M\omega$. Formally,

$$\begin{aligned} Q^{GW}(a_*, x) &\equiv \left. \frac{d^2 N}{dt d\omega} \right|_{s=2} \\ &= \sum_{plm} \frac{\gamma_{2lm}(a_*, M\omega)}{\exp((\omega - m\Omega)/T_H) - 1} \\ &= \sum_{plm} \frac{\gamma_{2lm}(a_*, x)}{\exp\left(4\pi \left[1 + (1 - a_*^2)^{-\frac{1}{2}}\right] x - 2\pi m a_* (1 - a_*^2)^{-\frac{1}{2}}\right) - 1}, \end{aligned} \quad (11)$$

where $T_H = \frac{1}{2\pi} \left(\frac{r_+ - M}{r_+^2 + a_*^2 M^2} \right)$ is the Hawking temperature. For gravitons, the number of polarizations p is 2.

Using the program described in the previous section, we calculated $Q^{GW}(a_*, M\omega)$ for 156 values of a_* from 0 to 0.99999, and 3000 values of x from 0.001 to 3.¹ For low a_* , only the several low- l modes are important. For each l , modes with different m 's make similar contributions, as spherical symmetry of the background is not severely distorted. For high a_* , angular momentum can be transferred from the BH to $m \approx l$ modes, and high- l modes become more important. For example, to keep $Q^{GW}(a_*, x)$ at a precision better than $\frac{1}{10^5}$, we considered modes with $l = 2, 3, 4, |m| \leq l$ for $a_* = 0$, and modes with $m = l = 2, 3, \dots, 14$ for $a_* = 0.99999$. Our results for the greybody factors are consistent with [11], and results for the total energy and angular momentum emission rates are consistent with [12].

Fig. (1) shows the graviton emission rates for $a_* = 0, 0.5, 0.9, 0.99999$. For a_* closer to unity, superradiance

causes enhanced emission and large particle energy range. In particular, each spike in $Q^{GW}(0.99999, x)$ corresponds to emission of one $m = l$ mode. Clearly, faster rotating BHs tend to emit more gravitons with higher energies. This is also the case for emission of other particles (though to a lesser extent), due to coupling between the spin of the particle and that of the hole. This happens for both bosons and fermions, even though superradiance happens only for boson fields, as explained in [18]. As a result, spin enhances the BH's total emission rate and thus reduces its lifetime, which will be seen in more detail in the next section.

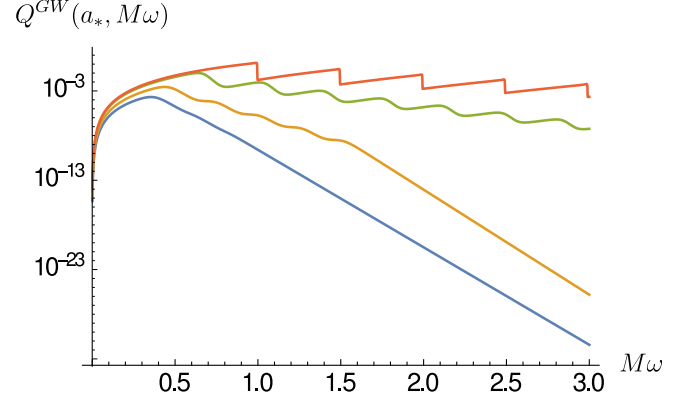


FIG. 1: Expected graviton emission rate vs. particle energy. From bottom to up, the curves correspond to $a_* = 0, 0.5, 0.9, 0.99999$ respectively. For $a_* = 0.99999$, five spikes from left to right originate from emission of $m = l = 2, 3, 4, 5, 6$ modes, respectively.

For each value of x , we used linear interpolation in x and cubic spline interpolation in $\kappa \equiv \frac{2}{1 + (1 - a_*^2)^{-1/2}}$ to get a smooth function $Q^{GW}(a_*, x)$. Fig. (2) shows this function for $x = 1, 2, 3$. This function will be used later in calculating today's graviton spectrum.

IV. EVOLUTION OF KERR BHS

Through Hawking radiation, BH's mass and angular momentum evolve with time. We use the dimensionless parameters f and g defined by Page [12] to trace the evolution of Kerr BHs,

$$\begin{aligned} f &\equiv -M^2 \frac{dM}{dt} \\ &= \sum_{splm} \int_0^\infty \frac{d\omega}{2\pi} \frac{\omega M^2 \gamma_{slm}(a_*, M\omega)}{\exp((\omega - m\Omega)/T_H) \pm 1} \\ &= \sum_{splm} \int_0^\infty \frac{dx}{2\pi} \times x \gamma_{slm}(a_*, x) \\ &\times \left[\exp\left(4\pi \left[1 + (1 - a_*^2)^{-\frac{1}{2}}\right] x - 2\pi m a_* (1 - a_*^2)^{-\frac{1}{2}}\right) \pm 1 \right]^{-1}, \end{aligned} \quad (12)$$

¹ The eigenvalues of spin-weighted spheroidal equation are calculated with a precision better than $\frac{1}{10^4}$ for $a_* x$ only up to 3, using the polynomial expansion to the 6th order.A

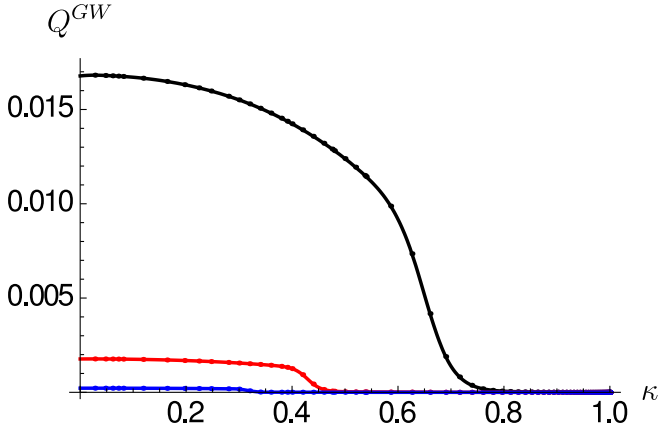


FIG. 2: Interpolated function Q^{GW} of $\kappa = \frac{2}{1+(1-a_*^2)^{-1/2}}$, for different x 's. From bottom to top, three sets of data points and smooth curves correspond to $x = 1, 2, 3$, respectively.

$$\begin{aligned}
 g &\equiv -\frac{M}{a_*} \frac{dJ}{dt} \\
 &= \sum_{splm} \int_0^\infty \frac{d\omega}{2\pi} \frac{m M a_*^{-1} \gamma_{slm}(a_*, M\omega)}{\exp((\omega - m\Omega)/T_H) \pm 1} \\
 &= \sum_{splm} \int_0^\infty \frac{dx}{2\pi} \times m a_*^{-1} \gamma_{slm}(a_*, x) \\
 &\times \left[\exp\left(4\pi \left[1 + (1 - a_*^2)^{-\frac{1}{2}}\right] x - 2\pi m a_* (1 - a_*^2)^{-\frac{1}{2}}\right) \pm 1 \right]^{-1}.
 \end{aligned} \tag{13}$$

Here the \pm signs account for different statistics of bosons and fermions. Functions f and g are measuring the rate of change of mass and angular momentum respectively. They depend on a_* only, as the greybody factors only depend on a_* and $x = M\omega$. We calculated the contributions to f and g from $s = 0, 2$, consistent with [13] and [12] respectively. For $s = 1/2, 1$, we just used the results in [12]. Tab. (I) lists all relevant f and g contributions.

Practically, we consider the number of degrees of freedom, i.e. the number of different particle species and polarizations, for scalars, spinors, vectors and tensors to be 1, 18, 2, 2 respectively as in the standard model². Then $f^{3/4}$ and $g^{3/4}$ are fitted as function of κ using 3rd order polynomial, with relative uncertainty below $\frac{1}{300}$ for all fitted parameters. The result is plotted in Fig. (3).

Once functions $f(a_*)$ and $g(a_*)$ are known, we can solve the evolution of BHs, from the definitions of f, g ,

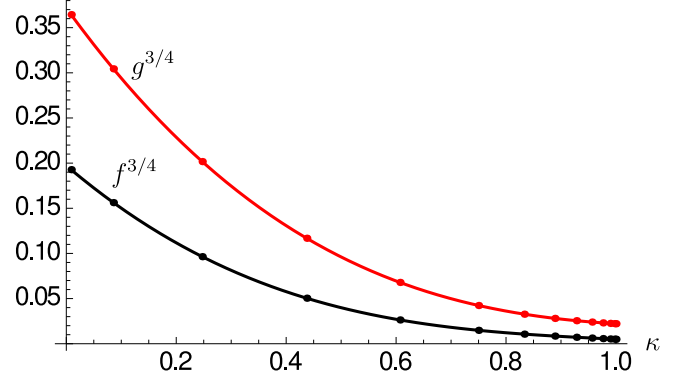


FIG. 3: The first fourteen values of $f^{3/4}$ and $g^{3/4}$ from Tab. (I) are fitted as third order polynomials in $\kappa = \frac{2}{1+(1-a_*^2)^{-1/2}}$. The fitted parameters all have uncertainties below $\frac{1}{300}$.

i.e. Eqs. (12, 13), which can be rewritten as

$$\begin{aligned}
 \frac{d \ln \bar{M}}{d \ln a_*} &= \frac{f(a_*)}{g(a_*) - 2f(a_*)} \\
 \frac{d\tau}{d \ln a_*} &= \frac{\bar{M}^3}{2f(a_*) - g(a_*)},
 \end{aligned} \tag{14}$$

where $\bar{M} \equiv M/M_i$ and $\tau \equiv t/M_i^3$. With initial conditions $\tau_i = 0$, $a_{*,i} = 0.99999$ and $\bar{M}_i = 1$, we solve Eqs. (14) for a_* down to 0.004. Thereafter, f, g are almost constant and we can use the analytic solution

$$\begin{aligned}
 \bar{M}(\tau) &= (const_1 - 3f(0)\tau)^{1/3} \\
 a_*(\tau) &= const_2 \times (\bar{M}(\tau))^{\frac{g(0)-2f(0)}{f(0)}},
 \end{aligned} \tag{15}$$

where $const_1, const_2$ are fixed by connecting with the previous numerical solution. There, an interval of 0.005 in $\ln a_*$ gives us a precision better than $\frac{1}{10^4}$.

Ten percent of the numerically solved data points are interpolated using cubic splines to form a smooth function $\bar{M}(\tau)$, which is shown in Fig. (4). Also shown is the BH evolution if $a_{*,i} = 0$, where Eqs. (15) are the solutions. For non-rotating BHs, the mass decay gets faster with time, because the Hawking temperature gets higher as the mass decreases. For Kerr BHs, on the other hand, the initial energy emission rate is high due to angular momentum transfer. Later, after the BH sheds its spin, the BH follows the history of Schwarzschild BHs.

Apparently, the BH's lifetime, denoted as τ_e , is shortened by its initial spin. For comparison, $\tau_e = 393.3$ for $a_{*,i} = 0$, while $\tau_e = 177.4$ for $a_{*,i} = 0.99999$.

V. CHOOSING PARAMETERS FOR PBH PRODUCTION

Two observational constraints are important in this context. First, the initial energy density in the universe

² For simplicity, we take one Higgs boson for scalars, all leptons for spinors, photons for vectors, and gravitons for tensors.

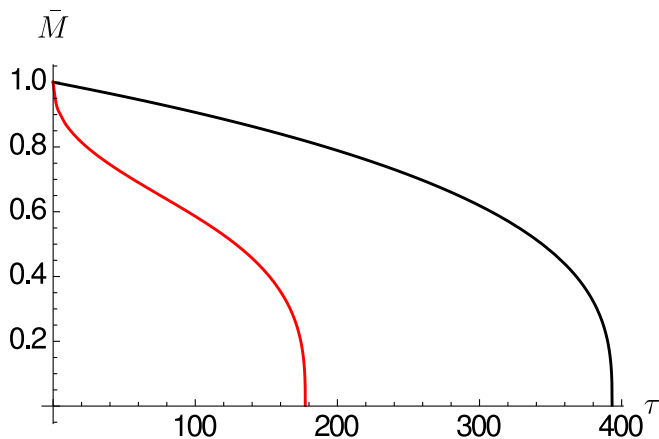


FIG. 4: The BH's mass evolution with time. The left curve is for $a_{*,i} = 0.99999$ and the right one for $a_{*,i} = 0$. In the beginning, the rotating BH loses mass more efficiently, due to its angular momentum transfer to particles. Near the end of evaporation, the BH has shed its spin, and so evolves in the same way as a Schwarzschild BH. This is why the two curves are nearly parallel as $\bar{M} \rightarrow 0$.

should be less than the energy scale at the end of inflation, i.e. $\rho_i \lesssim (10^{16} \text{GeV})^4$, due to non-detection of gravitational waves at that scale. Second, in order not to contradict cosmological observations, the safest assumption is that PBHs disappear before BBN [10] (we will relax this requirement later). We choose the temperature at BBN as when neutrinos began to decouple from the electrons, i.e. 10^{10}K . The total energy density at BBN is [19]

$$\rho_{BBN} = a_B T^4 + \frac{7}{8} \times 3a_B \left(\frac{T}{1.008} \right)^4 = (0.753 \text{MeV})^4, \quad (16)$$

where a_B is the Stefan-Boltzmann constant and $\frac{T}{1.008}$ is the temperature of neutrinos at that time. Therefore, we require that the total energy density at the end of PBH's evaporation, ρ_e , is higher than $(0.753 \text{MeV})^4$.

In the radiation-dominated universe, PBHs form when a sufficiently large density fluctuation falls into the particle horizon, so we take $M_i \leq \frac{4\pi}{3} \rho_i H_i^{-3}$, where the sign $<$ comes from the possibility that early phase transition can greatly enhance the formation of smaller PBHs [20]. For simplicity, the equal sign is taken in the following calculations. The initial collapse of density fluctuations might not be completely isotropic. As a result, the formed PBHs can possibly have non-zero angular momentum. In addition, accretion is very effective in spinning BHs up. The amount of accreted mass which is comparable to the initial BH mass is sufficient to spin up the BH from a non-rotating state to almost extremal Kerr state [21]. In the following, we consider PBHs in two extreme cases, i.e. $a_{*,i} = 0, 0.99999$, to illustrate the effect of the

BH spin.

In Sec. II we calculated the absorption probability (greybody factor) of BHs considering incoming waves at flat asymptotic infinity, which is satisfied only if $r_+ \ll d_{BH}$, where d_{BH} is the average physical distance between neighboring BHs. So we need $M_i \ll (\beta \rho_i / M_i)^{-1/3}$. Here β is the PBH mass fraction at formation. This is easily satisfied if $\beta \ll 1$. This is the third constraints that we will impose.

In the following, we discuss both PBHs which evaporated before BBN, and those which evaporated by today or still exist. For the former, we take $\beta = 10^{-2}, 10^{-4}, 10^{-8}, 10^{-16}$. For the latter, we take the upper bounds of observational constraints on β as a function of M_i , in order to get the largest possible signal of gravity waves. For simplicity, we will always assume a uniform initial mass distribution for PBHs forming at one certain epoch.

VI. COSMIC EXPANSION

The PBHs are evaporating in the expanding cosmos. Now we complete the link between the present-day observable spectra and the instantaneous emission rate $Q^{GW}(a_*, x)$.

From the graviton energy and density, we denote the present-day values with a tilde on the top, and their instantaneous values without. Consider a time interval dt and frequency interval $d\omega$, in which some amount of energy $d\omega dt \frac{dE}{dtd\omega}$ is emitted in gravitons. We have

$$\frac{d\rho_{GW}}{dtd\omega} = n_{BH} \frac{dE}{dtd\omega}, \quad (17)$$

where n_{BH} is the instantaneous number density of PBHs. This energy density of massless gravitons scales as a^{-4} as the universe expands, where a is the cosmological scale factor. We can then scale the graviton energy density to today $\tilde{\rho}_{GW} = \rho_{GW} a^4$.³ And its frequency ω is related to its redshifted today's value $\tilde{\omega}$ as $\tilde{\omega} = a\omega$. We ignore anisotropic stress from neutrino free streaming [22], since the wavelengths of the modes are much smaller than the Hubble length. We immediately get

$$\begin{aligned} dt \frac{d\tilde{\rho}_{GW}}{dtd\tilde{\omega}} &= dt a^3(t) n_{BH}(t) \frac{dE}{dtd\omega} \\ &= dt a_i^3 n_{BH,i} \frac{dE}{dtd\omega} \\ &= \frac{\beta \rho_i a_i^3}{M_i} dt \frac{dE}{dtd\omega}, \end{aligned} \quad (18)$$

where the second equality follows from $n_{BH} \sim a^{-3}$. The instantaneous graviton spectrum is related to the Q fac-

³ The cosmological scale factor today is taken to be 1.

tor as

$$\begin{aligned}\frac{dE}{dt d\omega} &= \frac{\omega}{2\pi} Q^{GW}(a_*(t), M(t)\omega) \\ &= \frac{\tilde{\omega}}{2\pi a(t)} Q^{GW}\left(a_*(t), M_i \tilde{\omega} \frac{\bar{M}(t)}{a(t)}\right).\end{aligned}\quad (19)$$

Here $\bar{M}(t)$ and $a_*(t)$ have already been solved in Sec. (IV). Integrating over t , we get

$$\begin{aligned}\Omega_{GW} &\equiv \frac{\tilde{\omega}}{\rho_c} \frac{d\tilde{\rho}_{GW}}{d\tilde{\omega}} \\ &= \frac{\beta a_i^3 \tilde{\omega}^2}{8\pi H_0^2} \int_0^{\tau_f} \frac{d\tau}{a(\tau)} Q^{GW}\left(a_*(\tau), M_i \tilde{\omega} \frac{\bar{M}(\tau)}{a(\tau)}\right),\end{aligned}\quad (20)$$

where ρ_c is the critical density of the universe, which is related to today's Hubble parameter H_0 by the Friedmann equation. $H_0 = h \times 100$ km/s/Mpc. h is left as a free parameter for PBHs evaporating before BBN, but it will be taken as the observed value of 0.673 for PBHs which completed evaporation only recently or are still evaporating today. The upper limit of integration τ_f is the PBH's lifetime τ_e if they've evaporated by today, or today's time otherwise.⁴ In order to calculate today's gravity wave spectrum Ω_{GW} , we need to know $a(\tau)$, which can be found from the Friedmann equation coupled with equations governing the evolution of the energy densities of PBHs and radiation, i.e.

$$\begin{aligned}\frac{d\rho_{BH}}{dt} &= -3\frac{\dot{a}}{a}\rho_{BH} + \rho_{BH}\frac{\dot{M}}{M}, \\ \frac{d\rho_{rad}}{dt} &= -4\frac{\dot{a}}{a}\rho_{rad} - \rho_{BH}\frac{\dot{M}}{M}, \\ \frac{\dot{a}}{a} &= \sqrt{\frac{8\pi}{3}(\rho_{BH} + \rho_{rad})}.\end{aligned}\quad (21)$$

Here dot overhead means the derivative with respect to cosmic time t . We will numerically solve Eqs. (21) in the following.⁵

VII. EVAPORATION BEFORE BBN (PBHS WITH $M_i \lesssim 10^9 g$)

The process of PBH formation is not fully understood, so we won't constrain ourselves to specific formation epoches (e.g. at early universe phase transitions [23–31]). Instead, in this section we will only require that

PBHs evaporate before BBN, after which the universe is radiation-dominated until matter-radiation equality. Therefore, for a given initial total energy density and PBH fraction, the production epoch (a_i) of PBHs will be fixed by the energy density right after evaporation, that is, $\rho_e a_e^4 = \rho_{BBN} a_{BBN}^4$.

The cosmological evolution before BBN is not well constrained, so we have freedom to choose the initial energy fraction of PBHs, not worrying that they can take over the dominance at some time before complete evaporation⁶. In the following, we shall choose it to be 10^{-2} , 10^{-4} , 10^{-8} , 10^{-16} . Also, we are interested in PBHs produced at various scales, so we shall choose several values for the initial total energy density, that is $\rho_i = 10^{-12}, 10^{-20}, 10^{-28}$. The unit of ρ_i is M_P^4 , where M_P is the Planck mass.

Using 4th-order Runge-Kutta method, we solved Eqs. (21). For each pair of (ρ_i, β) and initial scale factor $a_i = 1$, an interval of 0.1 in $\ln \tau$ for $\tau \leq 100$ and in τ for $\tau > 100$ gives us a precision better than $\frac{1}{10^6}$. In order to calculate the BH's signal observed at present, we need to know the initial scale factor relative to today's, a_0 . Take $a_0 = 1$, then at BBN,

$$a_{BBN} = \frac{T_{\nu 0}}{T/1.008} = 1.96 \times 10^{-10}, \quad (22)$$

where $T_{\nu 0} = 1.945 K$ is neutrino's temperature today.

If PBHs finished evaporation at some time t_e before BBN, we assume there was no phase change in the universe between this time and BBN. Thus we have $\rho_{rad,e} a_e^4 = \rho_{BBN} a_{BBN}^4$. Therefore, after numerical integration, we get the scale factor and radiation energy density at the end of evaporation (when $\rho_{BH,e}$ just vanished). We then determine the correct initial scale factor as $a_i = \left(\frac{\rho_{BBN} a_{BBN}^4}{\rho_{rad,e} a_e^4}\right)^{1/4}$.

The results of the evolution of energy densities, are shown for $\beta = 10^{-2}, 10^{-16}$ and $a_{*,i} = 0.99999$ in Figs. (5). With log-scales, the BH evaporation is only seen as a dip at the end of the solid curves.⁷ The cosmological scaling is clearly seen, i.e. $\rho_{BH} \sim a^{-3}$ and $\rho_{rad} \sim a^{-4}$. For $\beta = 10^{-16}$, PBHs never dominate, so the radiation-dominated universe evolves just as in standard cosmology. For $\beta = 10^{-2}$, however, PBHs take over the dominance before completing evaporation. Therefore, universe starting with different energy scales evolves along different curves.

⁴ Strictly, the integration lower limit is fixed by the total energy density at PBH's formation, i.e. $t_i = 1/(2H_i) = (32\pi\rho_i/3)^{-1/2}$. But $\tau_i = t_i/M_i^3$ is always very close to 0.

⁵ With certain simplified special assumptions on the form of PBH mass spectrum and of greybody factors, the above coupled equations can be analytically solved [32].

⁶ PBH mergers can largely increase their lifetime, easily making them survive after BBN. But the merger rate goes as β^{N-1} , where N is the number of PBHs which are merged, as estimated in [10]. We have chosen β to be no larger than 10^{-2} , so this effect can be safely neglected.

⁷ Also for this reason, the evolution for the case $a_{*,i} = 0$ has no visible difference with the $a_{*,i} = 0.99999$ case, thus not shown here.

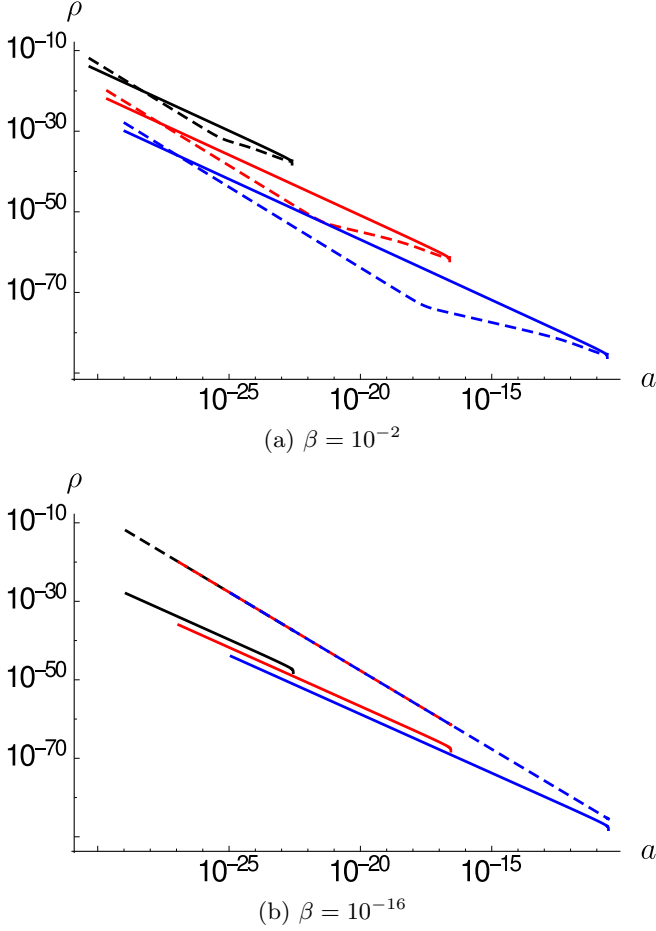


FIG. 5: Evolution of PBH (solid curves) and radiation (dashed curves) energy densities with the cosmological scale factor a , during the lifetime of PBHs, for $a_* = 0.99999$. The upper plot is for $\beta = 10^{-2}$, and the lower for $\beta = 10^{-16}$. Different colors denote different ρ_i 's. Black, red, blue curves are for $\rho_i = 10^{-12}, 10^{-20}, 10^{-28}$ respectively.

The data for (τ, a) is interpolated using cubic splines to get a smooth function $a(\tau)$, in order to do the integration in Eq. (20). The same discretization of τ as before is used to do 4th-order Runge-Kutta integration. The numerical error in Ω_{GW} is less than $\frac{1}{10}$, evaluated by halving the τ interval and comparing the results with those shown here. Today's gravity wave spectrum is shown in Figs. (6, 7, 8).

Fig. (6) shows the effects of the rotational parameter $a_{*,i}$. Within a certain range, higher $a_{*,i}$ enhances graviton emission by up to a factor of 10^3 . This enhancement gets less significant at lower frequencies, which is consistent with the trend in Fig. (1) that superradiance has smaller effects at lower ω . For high frequencies, however, higher $a_{*,i}$ produces marginally lower gravity wave signal. This is because PBHs are effectively Schwarzschild at late times, and the shorter PBH's lifetime for higher

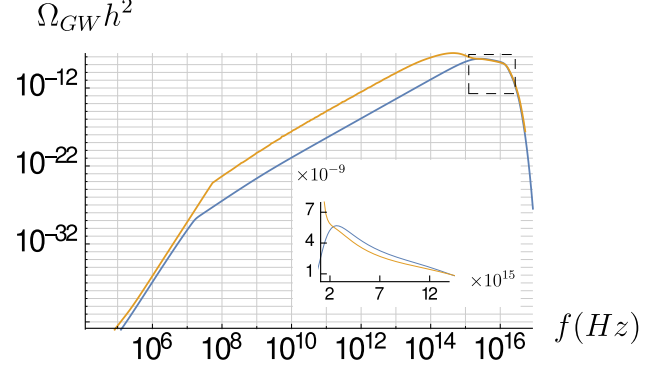


FIG. 6: Today's gravity wave spectrum, for $\rho_i = 10^{-12}$, $\beta = 10^{-2}$. Different colors denote different $a_{*,i}$'s. Blue and orange curves are for $a_{*,i} = 0, 0.99999$ respectively. The part within a dashed square is also shown in a linear-scale sub-plot. Note the dashed square is not the exact position of the sub-plot.

$a_{*,i}$ makes gravitons experience slightly higher redshifts.

Figs. (7) show the effects of the initial BH fraction β . Larger PBH fraction at production generally produces larger signals. This is most significant for not very high frequencies. Ω_{GW} is not proportional to β , because the cosmic history is also altered by the presence of PBHs. At the high ends of frequencies, this difference diminishes gradually, because the redshifts experienced by gravitons emitted near the end of PBH's evaporation are determined purely by the PBH's lifetime. For $\beta \geq 10^8$, PBHs dominate the universe near their end of life, so Ω_{GW} 's for different β converge. This convergence happens earlier for lower ρ_i , because PBHs evolve for a larger number of e-folds, making them easier to dominate before evaporation.

Figs. (8) show the effects of ρ_i . As before, more e-folds experienced by PBHs for lower ρ_i make the graviton's frequency f cover a larger range. Especially, the peak value of Ω_{GW} happens at a higher frequency. Also, as seen in Fig. (5), PBHs have larger energy density during their evaporation for larger ρ_i , thus producing a larger gravity wave signal today. This effect is more apparent for $\beta = 10^{-2}$ than for $\beta = 10^{-16}$, also consistent with Fig. (5).

The largest signal is produced in the case with $\rho_i = 10^{-12}$, $\beta = 10^{-2}$ and $a_{*,i} = 0.99999$. The Ω_{GW} amplitude reaches approximately $10^{-7.5}$ at $f \approx 4 \times 10^{14}$ Hz.

For comparison, our results agree well with [10] for Schwarzschild PBHs, where the greybody factors were assumed to be proportional to ω^2 without a full numerical calculation.

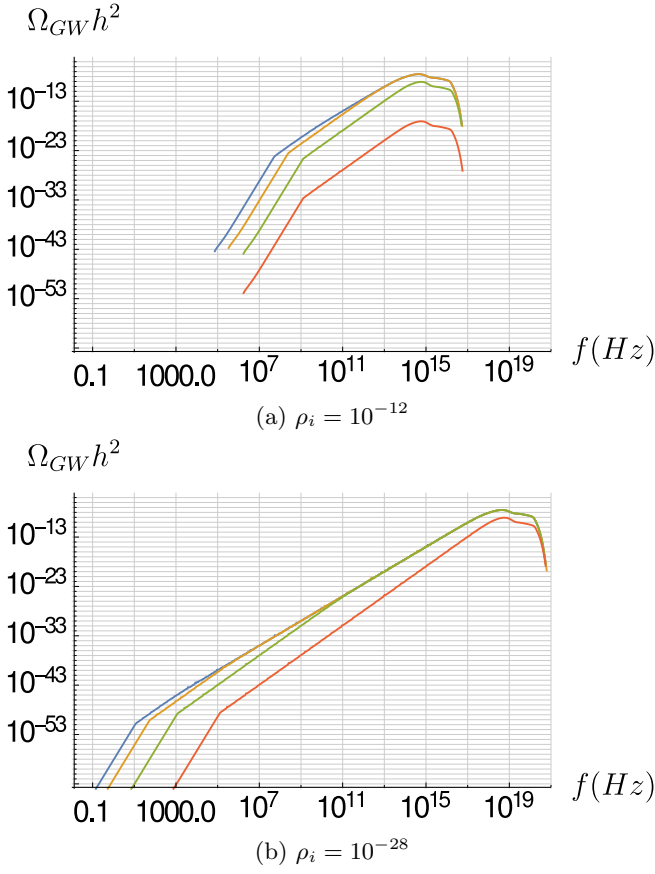


FIG. 7: Today's gravity wave spectrum, for $a_{*,i} = 0.99999$. $\rho_i = 10^{-12}$ for the upper plot, and $\rho_i = 10^{-28}$ for the lower one. In each plot, four curves from top to bottom, are for $\beta = 10^{-2}, 10^{-4}, 10^{-8}, 10^{-16}$, respectively.

VIII. CONSTRAINTS ON PBH'S INITIAL MASS FRACTION

While PBH which evaporate before the BBN are not seriously constrained, this is not so for PBH which evaporate later. In this section, we constrain the abundance of such PBHs at the time of their formation. The energy fraction of the universe in PBHs at their formation is well constrained from various observations [33–38], especially for small ones which have evaporated by today. We replot the most recent results [33] in the Fig. (9). The dip at the critical mass $M_i \approx 5 \times 10^{14}g$ corresponds to the PBH which just completed evaporation today. The physical meaning of the various constraints is explained below, and more details can be found in [33].

${}^4\text{He}$ abundance and D/H ratio for $M_i = 10^9 - 10^{10}g$: Some of the quarks and gluons emitted by PBHs fragment into mesons and antinucleons, which have enough time to get thermalized and then scatter with background nucleons, causing interconversion between protons and neutrons. As a result, this can increase the neutron/proton ratio, and thus change the ${}^4\text{He}$ and deu-

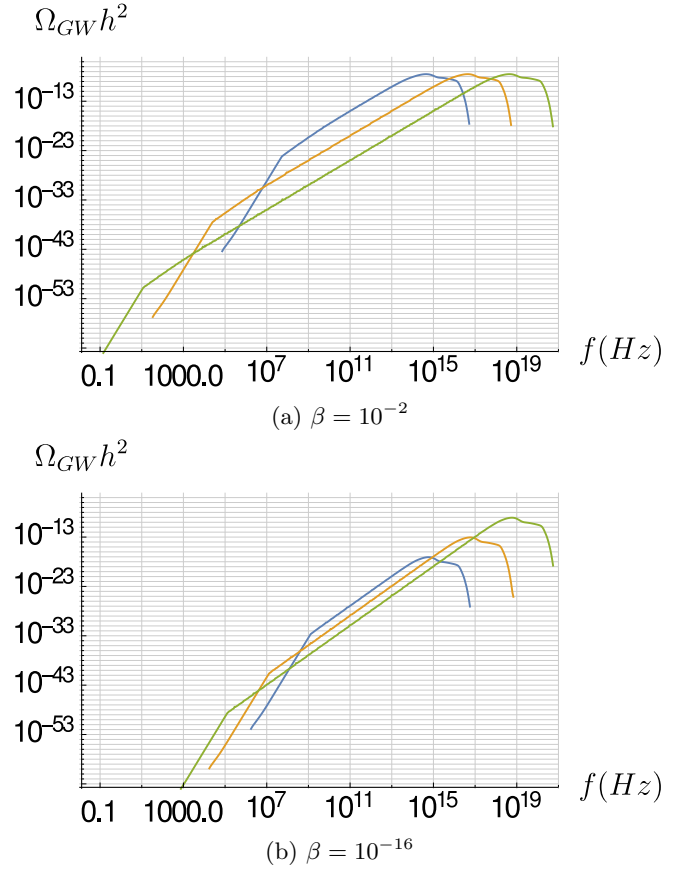


FIG. 8: Today's gravity wave spectrum for $a_{i,*} = 0.99999$. $\beta = 10^{-2}$ for the upper plot, and $\beta = 10^{-16}$ for the lower one. In each plot, blue, orange and green curves are for $\rho_i = 10^{-12}, 10^{-20}, 10^{-28}$, respectively.

terium, D , abundance. The observed ${}^4\text{He}$ abundances and D/H ratio thus set an upper limit on $\beta(M_i)$.

${}^6\text{Li}/{}^7\text{He}$ ratio for $M_i = 10^{10} - 10^{12}g$: High-energy nucleons, produced during the PBH evaporation and subsequent fragmentation, can scatter off background nuclei from BBN. Hadrodissociation produces energetic debris including tritium, T , and ${}^3\text{He}$, which then scatter with the nuclei background and result in extra production of ${}^6\text{Li}$. In this way, $\beta(M_i)$ can be constrained by the well observed ${}^6\text{Li}/{}^7\text{Li}$ ratio.

${}^3\text{He}/D$ ratio for $M_i = 10^{12} - 10^{13}g$: At the temperature of PBH evaporation, the produced energetic neutrons have time to decay before hadrodissociation, emitting photons with energies comparable to nuclei binding energy. So the photons can dissociate them and as a result, overproduce ${}^3\text{He}$ or D . The observation of the ${}^3\text{He}/D$ ratio thus constrains $\beta(M_i)$.

Diffuse extragalactic γ ray background for $M_i = 1.8 \times 10^{14} - 10^{17}g$: PBHs produce photons, both through direct Hawking radiation, and also through secondary processes involving the emitted quarks and gluons. The total γ ray spectrum should be within the spectrum of the dif-

fuse extragalactic γ ray background observed by HEAO 1, COMPTEL, EGRET and Fermi LAT. This gives an upper limit on $\beta(M_i)$.

Galaxy γ ray background for $M_i = 5 \times 10^{14} - 10^{15}g$: If there are PBHs residing our galactic halo, an anisotropic γ ray background will be produced. Requiring this spectrum to be consistent with the EGRET observation, we can get the constraints on $\beta(M_i)$.

Cosmic microwave background, CMB, for $M_i = 2.5 \times 10^{13} - 1.8 \times 10^{14}g$: The PBH's emission of electrons and positrons after recombination would cause the damping of small-scale CMB anisotropies, whose measurements thus constrains $\beta(M_i)$.

PBH's relic abundance, Ω_{PBH} , for $M_i \geq 10^{17}g$: For these nearly non-evaporating PBHs, this constraint comes from the requirement that today's PBH mass density is not larger than that of the cold dark matter.

Note that the above constraints are given for Schwarzschild PBHs, but in the following the same constraints will be assumed for Kerr PBHs since there are no constraints for rotating BHs published in the literature. We consider here PBHs with initial mass not above $10^{18}g$, above which the graviton signals will decrease with increasing initial masses, as will be shown.

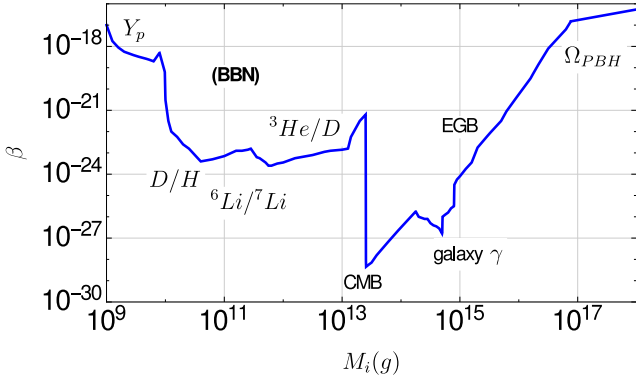


FIG. 9: Constraints on the PBH's mass fraction at the time of formation. The physical constraints are put below or above the corresponding segments. BBN: from the measurements of 4He abundance (Y_p), D/H ratio (D/H), $^6Li/^7Li$ ratio ($^6Li/^7Li$) and $^3He/D$ ratio ($^3He/D$); CMB: from CMB anisotropy measurements; EGB: from extragalactic gamma ray backgrounds; galaxy γ : from gamma ray emission in the local galaxy; Ω_{PBH} : from the energy fraction of PBHs existing today. For details, please refer to [33].

Under these constraints, PBHs are always subdominant before evaporation. So we can use the standard cosmology model instead of solving the coupled set of equations (21). The standard model parameters are taken as $h = 0.673$, $\Omega_m = 0.315$ and $\Omega_\Lambda = 0.685$ [39].

IX. GRAVITY WAVES FROM PBHS WITH $M_i \geq 10^9g$

These large PBHs have completed their evaporation after BBN, or are still evaporating today. Within the constraints on their initial mass fraction, we calculate the largest possible gravity wave signals. For this purpose, we choose PBHs corresponding to the local maximums in Fig. (9), and also $M_i = 10^{15}$, 10^{16} , 10^{17} and $10^{18}g$. For higher PBH masses, as shown later, the gravity wave signal is smaller.

PBHs with $M_i \lesssim 5 \times 10^{14}g$ have completed evaporation by today. The result for $M_i = 10^9$, 8×10^9 , 2.8×10^{11} , 2.5×10^{13} and $1.8 \times 10^{14}g$ is shown in Fig. (10). We only show the result for the case $a_{*,i} = 0.99999$. The difference with the $a_{*,i} = 0$ case is similar to that for GUT-scale PBHs in Fig. (6), so it is not shown here.

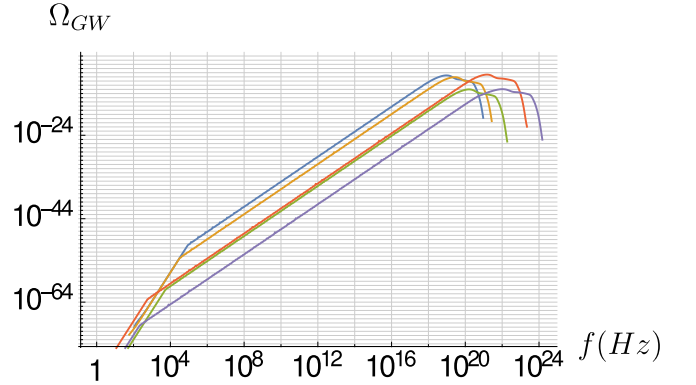


FIG. 10: Today's gravity wave spectrum from $M_i = 10^9g$ (blue), 8×10^9g (orange), $2.8 \times 10^{11}g$ (green), $2.5 \times 10^{13}g$ (red) and $1.8 \times 10^{14}g$ (purple). Here $a_{*,i} = 0.99999$, and β 's are taken as the upper limits in Fig. (9).

PBHs with $M_i \gtrsim 5 \times 10^{14}g$ still exist today. Using the constraints in Fig. (9), we get the spectrum in Fig. (11), for $M_i = 10^{15}$, 10^{16} , 10^{17} and $10^{18}g$. Ω_{GW} for $M_i = 10^{16}g$ is higher than that for $M_i = 10^{15}g$, because the latter is more strictly constrained, as seen from Fig. (9). With the same kind of constraints, the $M_i = 10^{18}g$ PBHs produce smaller signals than $M_i = 10^{17}g$ PBHs, because they have evaporated for a shorter time. For higher-mass PBHs, the calculated gravity wave signal is even smaller.

To see the effects of $a_{*,i}$, we plot the $M_i = 10^{17}g$ case also for Schwarzschild PBHs (Fig. (12)). The enhanced emission is clearly seen, especially in the high-frequency part. PBHs in that mass range have not shed their spin yet, so the two curves don't converge as in Fig. (6).

The largest amplitude of Ω_{GW} is around $10^{-6.5}$ for the case in which $M_i = 10^{17}g$ and $a_{*,i} = 0.99999$.

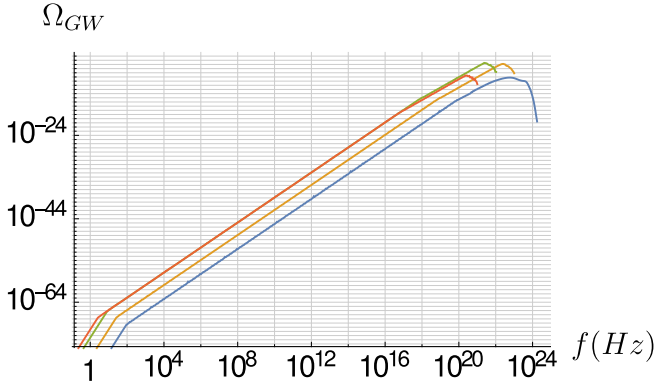


FIG. 11: Today's gravity wave spectrum from $M_i = 10^{15}\text{g}$ (blue), 10^{16}g (orange), 10^{17}g (green), $\times 10^{18}\text{g}$ (red). Here $a_{*,i} = 0.99999$, and β 's are taken as the upper limits in Fig. (9).

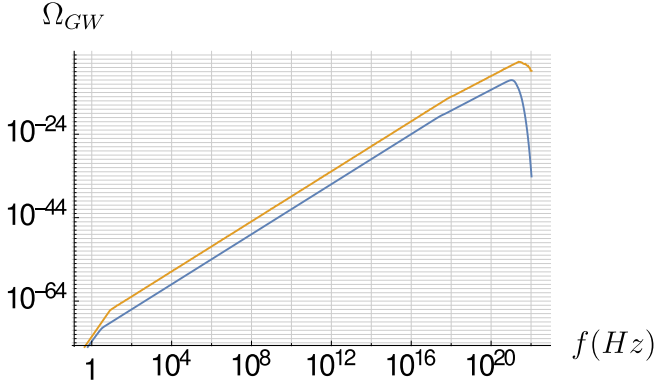


FIG. 12: Today's gravity wave spectrum from $M_i = 10^{17}\text{g}$ PBHs, with $a_{*,i} = 0$ (blue) and $a_{*,i} = 0.99999$ (orange). β is taken from the upper bound in Fig. (9).

X. CONCLUSIONS

In this paper we addressed the question of gravity wave production from evaporating PBHs. Such PBHs can emit a good fraction of their mass into gravitons, which can be today detected in the form of gravity waves. The spectrum of gravitational waves that can be detected today depends on multiple factors: fraction of the total energy density which was occupied by PBHs, the epoch in which PBHs are formed, and quantities like mass and angular

momentum of evaporating PBHs.

In our analysis we used the limits on the epochs in which PBHs are formed and the total energy density occupied by PBHs at the time of their formation from various astrophysical observations. We then calculated the greybody factors for emission of particles with various spins. These greybody factors strongly depend on the BH angular momentum and spin of emitted particles. Highly rotating BHs dominantly emit gravitons, while non-rotating PBHs dominantly emit scalar particles. However, angular momentum is shed faster than mass, so PBHs emit more lower spin particles toward the end of their lifetime.

The fact that gravitons are emitted early, while the PBH is still rotating fast, means that they are redshifted more than particles emitted later in the process of evaporation. We can see this enhanced graviton emission for higher a_* in the lower frequency parts of the spectra for PBHs which have evaporated by BBN or by today (Figs. (6)), as well as in the whole spectrum for PBHs existing today which have not shed their angular momentum yet. Another effect of initial angular momentum is that faster rotating PBHs, as a whole, tend to emitted more higher energy particles, thus having a shorter lifetime. But the largest graviton signal we can observe today is from the late stage of their evolution, because these gravitons experience smaller energy redshift. Therefore, for PBHs which have evaporated already, we see a marginally larger magnitude in the spectrum near the maximum for initially non-rotating PBHs than the fast rotating ones (Figs. (6)). We have examined the two cases for $a_* = 0$ and $a_* = 0.99999$, for $M\omega \leq 3$.

From the comprehensive analysis performed here, we conclude that very small PBHs which evaporate before BBN emit gravitons which can give the magnitude of the gravitational wave signal today of up to $10^{-7.5}$ (Fig. (6, 7, 8)). On the other hand, PBHs which are massive enough so that they are still evaporating today (and are still in agreement with the observational constraints) can yield a signal of magnitude as high as $\sim 10^{-6.5}$ (Fig. (11, 12)). However, typical frequencies of the gravity waves from these PBHs are still too high to be observed with the current and near-future gravity wave observations.

Acknowledgment

This work was also partially supported by the US National Science Foundation, under Grant No. PHY-1417317.

-
- [1] B. P. Abbott *et al.* [LIGO Scientific and Virgo Collaborations], Phys. Rev. Lett. **116**, no. 6, 061102 (2016) doi:10.1103/PhysRevLett.116.061102 [arXiv:1602.03837 [gr-qc]].
- [2] B. P. Abbott *et al.* [LIGO Scientific and Virgo Collaborations], Phys. Rev. Lett. **116**, no. 24, 241103 (2016)

- doi:10.1103/PhysRevLett.116.241103 [arXiv:1606.04855 [gr-qc]].
- [3] E. Bugaev and P. Klimai, Phys. Rev. D **83**, 083521 (2011) doi:10.1103/PhysRevD.83.083521 [arXiv:1012.4697 [astro-ph.CO]].
- [4] E. V. Bugaev and P. A. Klimai, JETP Lett. **91**, 1 (2010)

- doi:10.1134/S0021364010010017 [arXiv:0911.0611 [astro-ph.CO]].
- [5] B. J. Carr and S. W. Hawking, Mon. Not. Roy. Astron. Soc. **168**, 399 (1974).
- [6] J. D. Barrow, E. J. Copeland and A. R. Liddle, Phys. Rev. D **46**, 645 (1992). doi:10.1103/PhysRevD.46.645
- [7] J. D. Barrow and B. J. Carr, Phys. Rev. D **54**, 3920 (1996). doi:10.1103/PhysRevD.54.3920
- [8] B. J. Carr, Astrophys. J. **201**, 1 (1975). doi:10.1086/153853
- [9] M. Khlopov, B. A. Malomed and I. B. Zeldovich, Mon. Not. Roy. Astron. Soc. **215**, 575 (1985).
- [10] R. Anantua, R. Easther and J. T. Giblin, Phys. Rev. Lett. **103**, 111303 (2009) [arXiv:0812.0825 [astro-ph]].
- [11] S. A. Teukolsky and W. H. Press, Astrophys. J. **193**, 443 (1974).
- [12] D. N. Page, Phys. Rev. D **14**, 3260 (1976).
- [13] B. E. Taylor, C. M. Chambers and W. A. Hiscock, Phys. Rev. D **58**, 044012 (1998) doi:10.1103/PhysRevD.58.044012 [gr-qc/9801044].
- [14] S. A. Teukolsky, Astrophys. J. **185**, 635 (1973).
- [15] Fackerell, Edward D., and Robert G. Crossman. "Spin-weighted angular spheroidal functions." Journal of Mathematical Physics 18.9 (1977): 1849-1854.
- [16] W. H. Press and S. A. Teukolsky, Astrophys. J. **185**, 649 (1973).
- [17] R. Dong and D. Stojkovic, arXiv:1505.03145 [gr-qc].
- [18] D. C. Dai and D. Stojkovic, JHEP **1008**, 016 (2010) [arXiv:1008.4586 [gr-qc]].
- [19] Steven Weinberg, *Cosmology* (Oxford University Press, Oxford, 2008).
- [20] J. C. Niemeyer and K. Jedamzik, Phys. Rev. Lett. **80**, 5481 (1998) [astro-ph/9709072].
- [21] M.A. Abramowicz, J. P. Lasota, Acta Astronomica, **30**, no. 1, (1980), p. 35-39.
- [22] S. Weinberg, Phys. Rev. D **69**, 023503 (2004) [astro-ph/0306304].
- [23] S. G. Rubin, M. Y. Khlopov and A. S. Sakharov, Grav. Cosmol. **5**, 51 (2000) [hep-ph/0005271].
- [24] M. Y. Khlopov, R. V. Konoplich, S. G. Rubin and A. S. Sakharov, Grav. Cosmol. **2**, S1 (1999) [hep-ph/9912422].
- [25] M. Y. Khlopov, Res. Astron. Astrophys. **10**, 495 (2010) [arXiv:0801.0116 [astro-ph]].
- [26] B. J. Carr, astro-ph/0511743.
- [27] K. Jedamzik, Phys. Rev. D **55**, 5871 (1997) [astro-ph/9605152].
- [28] D. Stojkovic, K. Freese and G. D. Starkman, Phys. Rev. D **72**, 045012 (2005) [hep-ph/0505026].
- [29] D. Stojkovic and K. Freese, Phys. Lett. B **606**, 251 (2005) [hep-ph/0403248].
- [30] E. Bugaev and P. Klimai, Phys. Rev. D **90**, no. 10, 103501 (2014) doi:10.1103/PhysRevD.90.103501 [arXiv:1312.7435 [astro-ph.CO]].
- [31] E. Bugaev and P. Klimai, Phys. Rev. D **85**, 103504 (2012) doi:10.1103/PhysRevD.85.103504 [arXiv:1112.5601 [astro-ph.CO]].
- [32] J. D. Barrow, E. J. Copeland and A. R. Liddle, Mon. Not. Roy. Astron. Soc. **253**, 675 (1991).
- [33] B. J. Carr, K. Kohri, Y. Sendouda and J. Yokoyama, Phys. Rev. D **81**, 104019 (2010) [arXiv:0912.5297 [astro-ph.CO]].
- [34] A. M. Green and A. R. Liddle, Phys. Rev. D **56**, 6166 (1997) [astro-ph/9704251].

- [35] M. Ricotti, J. P. Ostriker and K. J. Mack, Astrophys. J. **680**, 829 (2008) [arXiv:0709.0524 [astro-ph]].
- [36] H. Tashiro and N. Sugiyama, Phys. Rev. D **78**, 023004 (2008) [arXiv:0801.3172 [astro-ph]].
- [37] B. J. Carr, Lect. Notes Phys. **631**, 301 (2003) [astro-ph/0310838].
- [38] P. Pani and A. Loeb, Phys. Rev. D **88**, 041301 (2013) doi:10.1103/PhysRevD.88.041301 [arXiv:1307.5176 [astro-ph.CO]].
- [39] K. A. Olive *et al.* [Particle Data Group Collaboration], Chin. Phys. C **38**, 090001 (2014). doi:10.1088/1674-1137/38/9/090001

Appendix A: Spin-weighted angular momentum

We will summarize ${}_sE_l^m$ for completeness. For the detailed derivation, see [15, 16]. For arbitrary helicity s , changing the variable from θ to $z \equiv \cos \theta$, the differential equation in question is

$$(1 - z^2) \frac{d^2 S}{dz^2} - 2z \frac{dS}{dz} + \left[\gamma^2 z^2 - \frac{m^2 + s^2}{1 - z^2} - \frac{2msz}{1 - z^2} - 2\gamma sz + {}_sE_l^m(\gamma) \right] S = 0, \quad (\text{A1})$$

where $\gamma = a_* M \omega$.

Define $\alpha \equiv |m + s|$, $\beta \equiv |m - s|$, we would like to express ${}_sE_l^m(\gamma)$ as a taylor series in γ ,

$${}_sE_l^m(\gamma) = \sum_{p=0}^{\infty} {}_s f_p^{lm} \gamma^p. \quad (\text{A2})$$

$${}_s f_0^{lm} = l(l+1), \quad (\text{A3})$$

$${}_s f_1^{lm} = -2s^2 m / l(l+1), \quad (\text{A4})$$

$${}_s f_2^{lm} = H(l+1) - H(l) - 1, \quad (\text{A5})$$

$${}_s f_3^{lm} = 2s^2 m \left[\frac{H(l)}{(l-1)l^2(l+1)} - \frac{H(l+1)}{l(l+1)^2(l+2)} \right], \quad (\text{A6})$$

$$\begin{aligned} {}_s f_4^{lm} = & 4s^4 m^2 \left[\frac{H(l+1)}{l^2(l+1)^4(l+2)^2} - \frac{H(l)}{(l-1)^2 l^4(l+1)^2} \right] \\ & + \frac{1}{2} \left[\frac{H^2(l+1)}{(l+1)} + \frac{H(l+1)H(l)}{l(l+1)} - \frac{H^2(l)}{l} \right] \\ & + \frac{1}{4} \left[\frac{(l-1)H(l-1)H(l)}{(l-1/2)l} - \frac{(l+2)H(l+1)H(l+2)}{(l+1)(l+3/2)} \right], \end{aligned} \quad (\text{A7})$$

$$\begin{aligned} {}_s f_5^{lm} = & 8s^6 m^3 \left[\frac{H(l)}{(l-1)^3 l^6(l+1)^3} - \frac{H(l+1)}{l^3(l+1)^6(l+2)^3} \right] \\ & + s^2 m \left[\frac{3H^2(l)}{(l-1)l^3(l+1)} - \frac{(7l^2 + 7l + 4)H(l)H(l+1)}{(l-1)l^3(l+1)^3(l+2)} \right. \\ & - \frac{3H^2(l+1)}{l(l+1)^3(l+2)} + \frac{1}{2} \left(\frac{(3l+7)H(l+1)H(l+2)}{l(l+1)^3(l+3/2)(l+3)} \right. \\ & \left. \left. - \frac{(3l-4)H(l-1)H(l)}{(l-2)(l-1/2)l^3(l+1)} \right) \right], \end{aligned} \quad (\text{A8})$$

$$\begin{aligned}
{}_s f_6^{lm} = & 16s^8 m^4 \left[\frac{H(l+1)}{l^4(l+1)^8(l+2)^4} - \frac{H(l)}{(l-1)^4 l^8(l+1)^4} \right] \\
& + 4s^4 m^2 \left[\frac{3H^2(l+1)}{l^2(l+1)^5(l+2)^2} - \frac{3H^2(l)}{(l-1)^2 l^5(l+1)^2} \right. \\
& + \frac{(11l^4 + 22l^3 + 31l^2 + 20l + 6)H(l)H(l+1)}{(l-1)^2 l^5(l+1)^5(l+2)^2} \\
& + \frac{1}{2} \left(\frac{(3l^2 - 8l + 6)H(l-1)H(l)}{(l-2)^2(l-1)(l-1/2)l^5(l+1)^2} \right. \\
& \left. - \frac{(3l^2 + 14l + 17)H(l+1)H(l+2)}{l^2(l+1)^5(l+3/2)(l+2)(l+3)^2} \right) \left. \right] \\
& + \frac{1}{4} \left[\frac{2H^3(l+1)}{(l+1)^2} + \frac{(2l^2 + 4l + 3)H^2(l)H(l+1)}{l^2(l+1)^2} \right. \\
& - \frac{(2l^2 + 1)H^2(l+1)H(l)}{l^2(l+1)^2} - \frac{2H^3(l)}{l^2} \\
& + \frac{(l+2)(3l^2 + 2l - 3)H(l)H(l+1)H(l+2)}{4l(l+1)^2(l+3/2)^2} \\
& - \frac{(l-1)(3l^2 + 4l - 2)H(l+1)H(l)H(l-1)}{4(l-1/2)^2 l^2(l+1)} \\
& + \frac{(l+2)^2 H^2(l+2)H(l+1)}{4(l+1)^2(l+3/2)^2} - \frac{(l-1)^2 H^2(l-1)H(l)}{4(l-1/2)^2 l^2} \\
& + \frac{(l-1)(7l-3)H(l-1)H^2(l)}{4(l-1/2)^2 l^2} \\
& - \frac{(l+2)(7l+10)H^2(l+1)H(l+2)}{4(l+1)^2(l+3/2)^2} \\
& + \frac{(l+3)H(l+1)H(l+2)H(l+3)}{12(l+1)(l+3/2)^2} \\
& \left. - \frac{(l-2)H(l-2)H(l-1)H(l)}{12(l-1/2)^2 l} \right]. \tag{A9}
\end{aligned}$$

.....

$$\text{Here } H(l) = \frac{[l^2 - (\alpha + \beta)^2/4][l^2 - s^2][l^2 - (\alpha - \beta)^2/4]}{2(l-1/2)l^3(l+1/2)}.$$

The above polynomial expansion to the 6th order is accurate within $\frac{1}{10^4}$ for γ up to 3.

Appendix B: f and g factors

a_*	f_0	$f_{1/2}$	f_1	f_2	g_0	$g_{1/2}$	g_1	g_2
0.01000	7.429×10^{-5}	8.185×10^{-5}	3.366×10^{-5}	3.845×10^{-6}	8.867×10^{-5}	6.161×10^{-4}	4.795×10^{-4}	1.064×10^{-4}
0.10000	7.442×10^{-5}	8.343×10^{-5}	3.580×10^{-5}	4.684×10^{-6}	9.085×10^{-5}	6.174×10^{-4}	4.895×10^{-4}	1.167×10^{-4}
0.20000	7.319×10^{-5}	8.830×10^{-5}	4.265×10^{-5}	7.732×10^{-6}	9.391×10^{-5}	6.218×10^{-4}	5.207×10^{-4}	1.514×10^{-4}
0.30000	7.265×10^{-5}	9.669×10^{-5}	5.525×10^{-5}	1.494×10^{-5}	1.024×10^{-4}	6.299×10^{-4}	5.759×10^{-4}	2.233×10^{-4}
0.40000	7.097×10^{-5}	1.089×10^{-4}	7.570×10^{-5}	3.116×10^{-5}	1.125×10^{-4}	6.430×10^{-4}	6.599×10^{-4}	3.603×10^{-4}
0.50000	6.996×10^{-5}	1.258×10^{-4}	1.080×10^{-4}	6.822×10^{-5}	1.281×10^{-4}	6.631×10^{-4}	7.845×10^{-4}	6.236×10^{-4}
0.60000	7.008×10^{-5}	1.487×10^{-4}	1.594×10^{-4}	1.574×10^{-4}	1.507×10^{-4}	6.946×10^{-4}	9.668×10^{-4}	1.155×10^{-3}
0.70000	7.119×10^{-5}	1.804×10^{-4}	2.450×10^{-4}	3.909×10^{-4}	1.803×10^{-4}	7.457×10^{-4}	1.245×10^{-3}	2.322×10^{-3}
0.80000	7.969×10^{-5}	2.284×10^{-4}	4.014×10^{-4}	1.104×10^{-3}	2.306×10^{-4}	8.366×10^{-4}	1.706×10^{-3}	5.286×10^{-3}
0.90000	1.024×10^{-4}	3.195×10^{-4}	7.520×10^{-4}	4.107×10^{-3}	3.166×10^{-4}	1.034×10^{-3}	2.632×10^{-3}	1.544×10^{-2}
0.96000	1.551×10^{-4}	4.567×10^{-4}	1.313×10^{-3}	1.305×10^{-2}	4.515×10^{-4}	1.343×10^{-3}	3.976×10^{-3}	4.057×10^{-2}
0.99000	2.283×10^{-4}	6.708×10^{-4}	2.151×10^{-3}	3.578×10^{-2}	6.160×10^{-4}	1.810×10^{-3}	5.829×10^{-3}	9.555×10^{-2}
0.99900	2.625×10^{-4}	9.253×10^{-4}	3.057×10^{-3}	7.251×10^{-2}	6.905×10^{-4}	2.340×10^{-3}	7.723×10^{-3}	1.753×10^{-1}
0.99999	2.667×10^{-4}	1.074×10^{-4}	3.555×10^{-3}	9.785×10^{-2}	6.997×10^{-4}	2.641×10^{-3}	8.730×10^{-3}	2.271×10^{-1}
1.00000	2.667×10^{-4}	1.093×10^{-4}	3.616×10^{-3}	1.012×10^{-1}	7.006×10^{-4}	2.678×10^{-3}	8.851×10^{-3}	2.338×10^{-1}

TABLE I: Contributions to f and g from each particle species. The first 14 lines are calculated, while the last one is from the cubic spline extrapolations. Please refer to the original papers [12, 13] for the calculations.